Title

Experimental and Numerical Study on Formation of Interface Separation and Interfacial Dielectric Strength of GIL Insulator

Journal

IEEE Transactions on Dielectrics and Electrical Insulation, 26(6)

ISSN

1070-9878

Authors

Guo, Zihao
Wu, Zehua
Wang, Haoran
et al.

Publication Date

2019-12-01

DOI

10.1109/tdei.2019.008060

Peer reviewed

Experimental and Numerical Study on Formation of Interface Separation and Interfacial Dielectric Strength of GIL Insulator

Zihao Guo, Zehua Wu, Haoran Wang, Huidong Tian, Lilan Liu and **Zongren Peng**
Xi'an Jiaotong University
State Key Laboratory of Electrical Insulation and Power Equipment
Xi'an, Shaanxi 710049, P.R.China

He Li and **Qing Wang**
The Pennsylvania State University
Department of Materials Science and Engineering
University Park, PA 16802, USA

ABSTRACT

As the transmission capacity of gas insulated transmission line (GIL) increases, the synergistic improvement in dielectric and mechanical strengths of GIL insulators is urgently needed for the development of advanced power systems. Mechanical defects in power equipment are prone to induce discharges during high voltage operations, which need to be mitigated. In this paper, the strains on the GIL insulator surface are measured by fiber Bragg grating (FBG) strain sensors during hydrostatic tests. An abnormal change of strain is detected near the interface between center conductor and the spacer. The numerical results of stress distributions of GIL insulator during manufacturing and high-voltage operation are calculated by the finite element method. The results indicate that the mechanical stresses are concentrated at the interface, which lead to the development of conductor-spacer interface separation. In addition, based on the hydrostatic test and the FEM calculations, the dielectric interfacial strength, including the electric field distribution, and flashover are investigated by a combination of numerical and experimental studies. The results indicate that the air gaps generated by the separated interface distort the electric field at the tip of the gap, which is likely to cause discharges and reduce the gas-solid interfacial flashover strength of the insulator, placing concerns of insulation failure and even operating failures of GIL. This work sheds light on the importance of interfacial structure of power equipment and will guide the design and the manufacture of GIL insulator.

Index Terms —**GIL insulator, fiber Bragg grating, stress concentration, interface separation, interfacial dielectric strength**

1 INTRODUCTION

GAS insulated transmission line (GIL) exhibits numerous advantages including high reliability in long-distance power transmission, long service life, high transmission capability and low energy loss. More importantly, GIL has lower requirements for transmission corridors in comparison with traditional overhead lines, which can be used for long-distance power transmission in complex terrains [1,2].

Insulators in GIL play important roles in the support of the high voltage conductor and the separation of different chambers. With the increase of transmission capacity, the size of the transmission conductor and insulation component increase significantly. Therefore, enhanced dielectric strength of the insulating components is critical for UHV GILs. During high voltage operation, the defects of the GIL insulator especially at the interface between different materials may distort the electric field, resulting in partial discharge (PD). Long term discharge will generate penetrating discharge channels, and even lead to the damage of the GIL insulator [3-5]. Xiong *et al* studied a 500 kV GIL substation failure that took place in the Daya Bay station. A discharge channel was found on the surface of the GIL spacer from the center to the edge and metal particles were found near the interface of the center conductor and spacer which confirmed the reason for the failure [6]. Mansour *et al* studied the PD and its associated mechanisms of GIS spacers. Their results suggested that PD occurs at multiple locations in the delamination gap [7,8]. Genyo *et al* studied the insulation characteristics of epoxy-based insulator with several types of micro-defects, including cracks,

Manuscript received 17 January 2019, in final form 9 April 2019, accepted xx Month 20yy. Corresponding author: Q. Wang.

voids and delaminations. Of all types of defects, their results showed that cracks give rise to the lowest puncture voltages [9,10]. Umemura *et al* studied the PD behavior of metal air-gap metal and metal air-gap insulation electrode systems and proposed the PD mechanism in small air-gap regions [11].

In addition to high-insulation performance, high mechanical strength is also critical for UHV GILs. However, few studies have focused on mechanical issues especially the interfacial mechanical strength of GIL insulators. During casting of GIL insulators, internal stress is generated in the body of the spacer due to the curing and cooling stages. In addition, during operation, the spacer is subjected to SF_6 at the operational pressure and in the installation and maintenance, GIL insulators face an unbalanced single-sided pressure from the SF_6 gas. The stress concentration caused by the aforementioned conditions may introduce mechanical defects such as cracks in the GIL insulators, which will affect the distribution of electric field [12,13]. In order to examine the mechanical strength of GIL insulator, hydraulic tests are used as a routine test during manufacturing. A hydrostatic test simulates installation or power maintenance that a single-sided pressure is applied on the spacer. The detected strains and the ultimate failure morphologies of the spacer help to evaluate the mechanical strengths of GIL insulator [14].

We first studied the possible defects and failure patterns of the GIL insulator by a hydraulic test. Through the analysis of measured strains and failure morphologies, it is found that the failure channel of the GIL insulator generates initially from the interface between the center conductor and spacer. We then studied the mechanical strain distribution of GIL insulators using finite element (FEM) method. The calculation results are accordance with the hydraulic test data, providing evidence that the stress is concentrated near the interface. Stress concentrations produce interface defects such as air-gaps, during operation. Additionally, the influence of air-gaps on interfacial dielectric properties were studied via both FEM calculations and experiments. The calculation results indicate that the air gap at the interface between the center conductor and spacer will distort the electric field, causing the maximum electric field strength to increase and the field to be concentrated at the interface. The flashover results show that the airgap at interface reduces the flashover voltage, which provides evidence that the mechanical separation of GIL spacer will decrease the interfacial dielectric strength.

2 MEASUREMENT ON STRAIN OF GIL INSULATOR IN HYDROSTATIC TESTS

Figure 1 shows two failed insulators during operation of GIS/GIL. In Figure 1a, the damaged UHV insulator which operated for less than one year, shows a large area of carbonization of the epoxy/Al_2O_3 composite body near the center conductor, and cracks in the spacer from the high voltage conductor to the flange. In Figure 1b, a regular linear crack was found in the UHV insulator and this failure occurred after a three-year operation. Different from surface discharge, the discharge appears inside these two insulators. More seriously, penetrating cracks were found in both insulators from center conductor to the flange. The discharges indicate that the mechanical weakness may lead to defects and initiate cracks even discharges in GIL insulators. Therefore, the mechanical strength of GIL insulators needs to be studied to find the potential defects inside insulators.

Figure 1. Two GIS/GIL insulator failures during operation.

A hydrostatic test can simulate the situation of applying single-sided pressure on spacer in installation and power maintenance. In order to study the strain distribution and to discover potential defects of the GIL insulator, the strain on the surface of spacer was measured by strain sensors at selected positions, and the failure morphology of GIL insulator was analyzed.

Fiber Bragg grating (FBG) sensors are utilized to measure the strain on the surface of spacer. FBG sensor has strong anti-interference ability and is more flexible than traditional strain sensors that can effectively reflect the cracks and damage of a GIL insulator through a sudden change of the strain during the hydraulic test [15]. The structure and the arrangement of FBG sensors are shown in Figure 2.

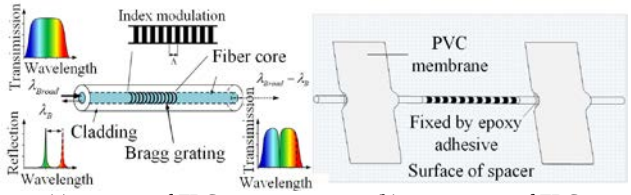

(a) structure of FBG (b) arrangement of FBG

Figure 2. The structure and the arrangement of FBG sensor.

FBG sensor converts strain and temperature signals into optical signals by changing the refractive index of the grating. A section of optical fiber is carved into a grating area according to the periodic distribution of refraction rate [15-17]. When a light beam with broad wavelength range transports into the grating, the light with a specific wavelength λ_B will be reflected. The λ_B satisfies the relation of Equation (1).

$$\lambda_B = 2n_{eff}\Lambda \tag{1}$$

where λ_B is the wavelength of reflected light, n_{eff} is the mean effective refractive index, Λ is the grating period of FBG.

Changes in temperature or strain will lead to the changes of effective refractive index and grating period of the FBG sensor, resulting in a change in the final reflection wavelength in the FBG sensor. If the temperature remains constant and the strain exists only in the axial direction of the fiber, the center wavelength λ_B of the reflected light will produce a change as the Equation (2) demonstrates.

$$\Delta\lambda_B = \lambda_B(1-P_k)\Delta\varepsilon \tag{2}$$

where ε is the axial strain, P_k is the effective optical strain constant, which is related to the properties of the optical fiber itself. When $\lambda_B(1-P_k)$ equals to k_ε, Equation (2) turns into $\Delta\lambda_B$

$= k_\varepsilon \cdot \Delta\varepsilon$, where k_ε is the strain factor and was collected in our previous study with a value of 921.66 nm [18]. The change in the center wavelength of reflected light is measured by a demodulator, and the strain is calculated accompanied with k_ε.

In the measurement, both sides of the FBG sensor are fixed on the surface of the spacer with adhesives as Figure 2b demonstrated. The change of strain on the spacer surface is converted into the change of the optical fiber. Ten FBG sensors are fixed on the convex surface of the spacer as in Figure 3. Since the spacer is axisymmetric, the radial and the circular strains are considered. Five sensors are arranged in radial direction and marked as R1, R2, R3, R4 and R5, the other five sensors are arranged in circular direction and marked as C1, C2, C3, C4 and C5. The distance of each point from the center conductor is 45, 145, 250, 330 and 445 mm.

Figure 3. The experimental set-up of the hydrostatic test.

The experimental set-up of the hydrostatic test is illustrated in Figure 3 and the GIL insulator is arranged in a base chamber with concave side up and fixed by several bolts with the base chamber. The FBG sensors are led out through the base chamber and connected to the demodulator.

The concave surface of the spacer is filled with water as the load and the basic stage of hydrostatic test process is shown in Figure 3. During the test, the fiber-optic demodulator records the changes of the center wavelength of the reflected light and the hydraulic pressure is recorded with time.

The hydrostatic test consists of three steps: load, hold, and unload. The hydraulic pressure is applied to the spacer surface uniformly which increases at a speed of 0.4 MPa/min, then held at the maximum pressure at this stage. Then the hydraulic load is released to zero at a rate of 2 MPa/min. The tests are performed repeatedly with a stepped increase in the maximum hydraulic pressure at each stage until damage to the insulator appears. The maximum loading of hydraulic pressure in each step starts from 1.2 MPa, and increases to 2.6 MPa with a step-increase of 0.2 MPa. At the final stage, the hydraulic loading increases at a rate of 0.4 MPa/min until failure of the GIL insulator.

Prior to applying the pressure of 2.2 MPa, the strains measured by all sensors show linear relationship with the hydraulic loading. When the hydraulic loading applied on the insulator reaches 2.2 MPa, the strain measured by C1 and R1 sensors, which are the closest to the center conductor exhibits the greatest changes in slope compared with other sensors. The strain measured by C1 and R1 are studied in detail and shown in Figure 4. Notably, the strains measured by C1 and R1 sensors show abnormalities of sudden change with the increase of loading.

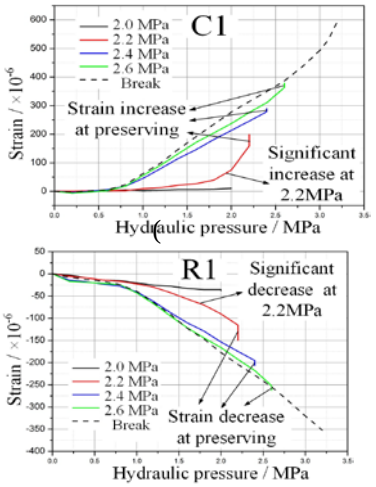

(a) (b)

Figure 4. Strain of (a) C1 and (b) R1 sensors when abnormality occurs.

It can be concluded from Figure 4 that the strain measured by C1 sensor increases and the strain measured by R1 sensor decreases with the increase of hydraulic pressure. The circular strain measured by C1 sensor shows a linear relationship with increasing hydraulic pressure before achieving 2.2 MPa. However, when the test is conducted in the stage where the maximum pressure is 2.2 MPa, the circular strain measured by C1 sensor shows a significant increase with the increase of hydraulic pressure, and the slope of the strain curve also increases gradually. Moreover, the strain keeps increasing while the hydraulic pressure is held constant. Accordingly, a similar change occurs on the radial strain measured by R1 sensor, that the radial strain of R1 shows a linear relationship with increasing hydraulic pressure before achieving 2.0 MPa. However, when the test is conducted in a stage where the maximum pressure is 2.2 MPa, the radial strain measured by R1 sensor shows a remarkable decrease with the increase of hydraulic pressure, and the slope of the strain curve decrease gradually. In addition, the circular strain measured by C1 sensor at the same hydraulic pressure increases with the repetition of the test.

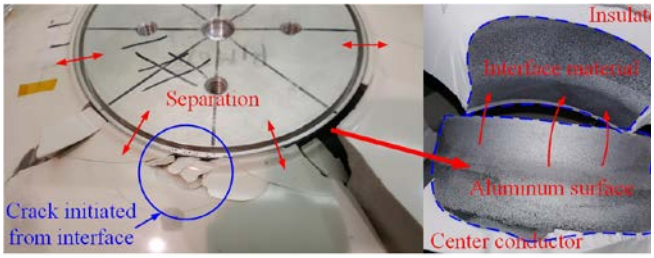

(a) Cracks on the spacer (b) Separation of the interface

Figure 5. The morphologies at the interface.

After the stage of the maximum applied pressure of 2.6 MPa, the hydraulic pressure keeps increasing until the final damage of GIL insulator occurs. Figure 5 illustrates the interfacial morphologies of the interface between the center conductor and spacer of a damaged GIL insulator.

As Figure 5a shows, there are many tiny cracks on the surface of the spacer near the interface between the center conductor and spacer. Also, the spacer materials (epoxy composite) are broken into small pieces. It can be inferred that the failure of the whole insulator generates initially from the

interface between the center conductor and spacer and the cracks develop from the interface to the edge of the spacer. Figure 5b shows that the aluminum conductor is completely exposed and the interface materials are attached on the insulator side, which indicate that the aluminum and epoxy composite are separated.

It can be concluded that defects may be formed at the interface between the center conductor and spacer during the hydraulic test, resulting in the interfacial mechanical weakness and the failure of the whole GIL insulator.

3 CALCULATION ON THE MECHANICAL PROPERTIES OF GIL INSULATOR

In order to analyze the forms and the causes of the defects at the interface between the center conductor and spacer, the stress distribution of insulators is analyzed by FEM calculation. The stress of GIL insulators mainly comes from two aspects: the internal stress generated during the casting processes and the pressure of SF_6 gas in the GIL. The combination of two kinds of stress may lead to the stress concentration in GIL insulator. The stress distribution of GIL insulator is calculated and the stress concentration phenomenon of insulators is studied by considering both influence factors.

3.1 CALCULATION METHOD

Each part of the object interacts with each other under the loading, and the stress in different directions is decomposed at a certain point. At this point, a micro-tetrahedron with unit vector of v is taken as Figure 6 shows.

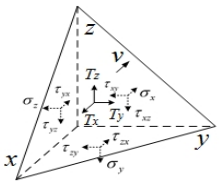

Figure 6. Micro-tetrahedron taken from the object.

When the area d_A of the slanted surface approaches to zero, a relationship between the stress vector components T_x, T_y, and T_z at this point as follows:

$$\left.\begin{aligned} T_x &= \sigma_x l + \tau_{yx} m + \tau_{zx} n, \\ T_y &= \tau_{xy} l + \sigma_y m + \tau_{zy} n, \\ T_z &= \tau_{xz} l + \tau_{yz} m + \sigma_z n, \end{aligned}\right\} \quad (3)$$

The Hooke's theorem gives the relationship between stress and strain, for unidirectional tension and pressure, the strain $\varepsilon = \sigma / E$, and $\gamma = \tau / G$ for pure shear problems. Equation (4) is obtained by promoting the Hooke's theorem.

$$\left.\begin{aligned} \varepsilon_x &= [\sigma_x - \mu(\sigma_y + \sigma_z)/E],\ \gamma_{xy} = \tau_{xy}/G \\ \varepsilon_y &= [\sigma_y - \mu(\sigma_x + \sigma_z)/E],\ \gamma_{yz} = \tau_{yz}/G \\ \varepsilon_z &= [\sigma_z - \mu(\sigma_x + \sigma_y)/E],\ \gamma_{xz} = \tau_{xz}/G \end{aligned}\right\} \quad (4)$$

The increase and the decrease of temperature in the elastic body will cause the volume expansion and contraction. In a differential cuboid with an edge length of d_x, d_y, d_z of the elastic body, the initial temperature is set as τ_0, and the real-time temperature is τ. If this differential element body is not constrained by other parts of the same object, the three edges will produce the same positive strain $\alpha(\tau - \tau_0)$ due to the isotropic nature of material. When the materials with different thermal expansion coefficients are contacted, the stress distribution within the object can be obtained based on the generalized Hooke's theorem.

3.2 CALCULATION MODEL

During the casting processes in manufacture of GIL insulators, the generated internal stress mainly consists of two parts: For one thing, chemical reactions including pre-polymerization and cross-linking during the curing process will generate internal stresses within the composite. For another, different thermal expansion coefficient of different materials may lead to the stress concentration at the interface between aluminum and epoxy composite during cooling process. Since the internal stress generated by the curing reaction is smaller than that caused by cooling [19], only the internal stress caused by cooling is considered in this study.

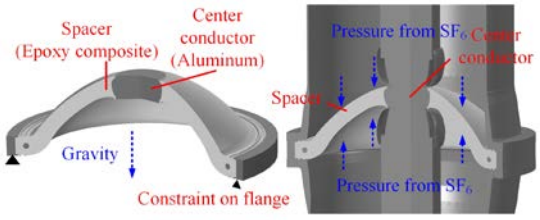

(a) casting (b) operation

Figure 7. The calculation model of GIL insulator of loading on the surface.

The finite element simulation software (Ansys) was used and the calculation model is shown in Figure 7. The flange is constrained and the effect of gravity is considered. The cooling temperature decreases from 130 to 30 ºC based on the industry manufacturing processes as Figure 7a shows. During operation, the spacer endures the pressure from SF_6 on both sides as Figure 7b shows, in the process of installation and power maintenance, the GIL insulator will face an unbalanced single-sided state pressure from SF_6 gas which is likely to cause stress concentration. The calculation is focused on the stress distribution of spacer with single-sided pressure, which is also used to verify the strain measured in hydraulic test. SF_6 with a gas pressure of 0.45 MPa is used as the insulating gas in engineering applications [20]. SF_6 pressure may be unstable during inflation and deflation processes, according to the routine test, in which a loading of 1 MPa is applied on the surface of spacer. Since the linear elastic material parameter is used for the calculation, the loading value will not affect the stress distribution of insulator.

The cross section of GIL insulator model was utilized for the calculation because of the insulator is in an axisymmetric structure. The thermal expansion coefficient and elastic modulus of epoxy composite applied in the calculation are measured by laser thermal dilatometer (Netzsch LFA447) and electronic universal testing machine (Wance TSE504C), which are assigned with temperature. The center conductor and flange are made of aluminum, whose elastic modulus and linear expansion coefficient do not change much within the

temperature range. Thus, the parameters of aluminum are set as constants in the calculation, elastic modulus E is 70 GPa, linear expansion coefficient α is 23.2×10^{-6} K^{-1}, Poisson's ratio μ is 0.33. In addition, the internal stress of epoxy composite during casting is also considered in calculation.

3.3 CALCULATION RESULTS

Figure 8a demonstrates the distribution of 1st principal stress inside the epoxy composite during casting. Compared with aluminum, the greater thermal expansion coefficient of epoxy composite leads to the larger volume shrinkage during the cooling processes. Therefore, there is a significant stress concentration at the interface between the aluminum and epoxy composite. The 1st principal stress in the whole GIL insulator is concentrated at the interface between the center conductor and spacer (near the convex surface).

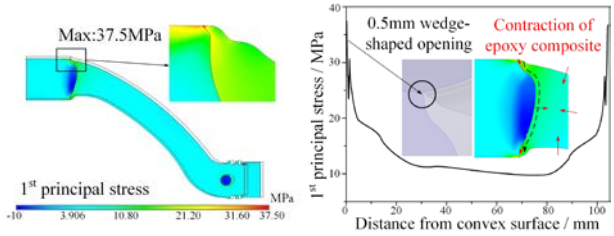

(a) stress distribution (b) stress on the center conductor

Figure 8. The distribution of internal stress caused by casting.

The maximum 1st principal stress is 37.5 MPa. The relationship between 1st principal stress and the distance from the convex surface along the interface is shown in Figure 8b. The relatively larger values of 1st principal stress is obtained near the convex and concave surface of the spacer interface. The contraction of epoxy composite is greater than that of aluminum. When the epoxy composite contracts toward the center, there exists stress in normal direction from the spacer to the center conductor. Meanwhile, the contractions of the epoxy composite itself generate the stress in tangential direction along the surface of center conductor, which will also lead to the shear stress concentration at the interface near the surface of the spacer. There has a 0.5 mm wedge-shaped opening near the surface of the spacer due to the manufacture processes, where the stress in tangential direction achieves the maximum along the center conductor, so the 1st principal stress also achieves the maximum.

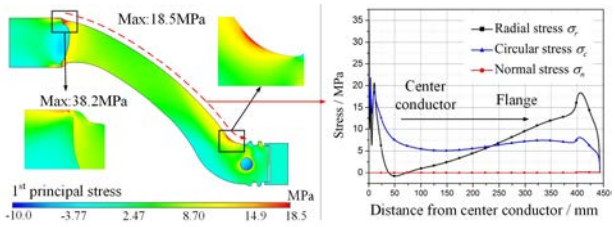

(a) stress distribution (b) stress on the convex surface

Figure 9. The distribution of stress caused single-side pressure.

The maximum stress is obtained by applying loading on concave surface of the spacer rather than applying loading on convex surface, thus a severe condition of applying single-sided pressure on the concave surface of spacer is considered. Figure 9a demonstrates the distribution of the 1st principal stress of GIL insulator when the concave surface is subjected to the loading of 1 MPa. The stress distribution concentrates on the surface of the spacer, and the stress at the convex surface is more significant than that of the concave surface. The stress distribution near the center conductor of the GIL insulator is similar to that of the internal stress caused by casting, where the maximum 1st principal stress is 38.2 MPa. In order to correspond to the strain measurement, the stress on the convex surface of the spacer is decomposed in the direction of radial, circular and normal. The relationship between the decomposed stress and the distance from center conductor is shown in Figure 9b. As illustrated in Figure 9b, the radial stress initially decreases rapidly to a bottom and then increases slightly to the maximum before falling rapidly to zero. The circular stress dropped from around 20 MPa to 5 MPa, and then basically maintains stable before decreasing to zero. The normal stress basically remains zero.

It can be concluded that there exists stress concentration at the interface between the center conductor and spacer during casting and operation, which may lead to the defects such as tiny cracks and interface separation of GIL insulator.

4 DISCUSSION ON FORMATION OF INTERFACE SEPARATION

Once there exists cracks inside spacer body materials, the insulator will easily be damaged with the increase of the hydraulic loading. However, during the hydrostatic test, the insulator can maintain a certain mechanical strength when the hydraulic loading is applied repeatedly after the abnormality occurred [21]. Meanwhile, no obvious abnormality of strain is found away from the interface, and the failure loading of the GIL insulator still can reach to 3.2 MPa without cracks in spacer body during the abnormality.

Semi-conductive coatings are often used at the interface between the center conductor and spacer to shield the defects such as bulges and glitches on the aluminum caused by manufacture [22,23]. The introduction of the semi-conductive coating builds a new interface between center conductor and spacer, thus will increase the possibility of the existence of mechanical interface defects. One of the main interface defects is separation, which caused by stress concentration especially the shear stress. In order to study the interface separation, the shear stress at the interface is calculated and the result is shown in Figure 10.

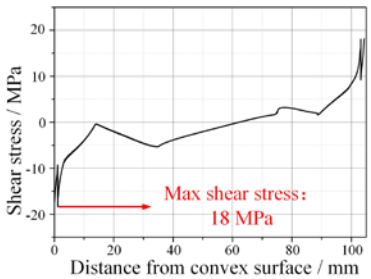

Figure 10. The shear stress distribution at the interface before abnormality.

Figure 10 demonstrates the shear stress distribution at the interface under a hydrostatic loading of 1 MPa. The maximum shear stress is obtained at the interface between the center conductor and spacer (near the convex surface of the spacer) and the value is about 18 MPa. With the increase of the

hydraulic pressure, the concentrated stress especially shear stress at the interface near the convex surface may lead to the failure of interface coating.

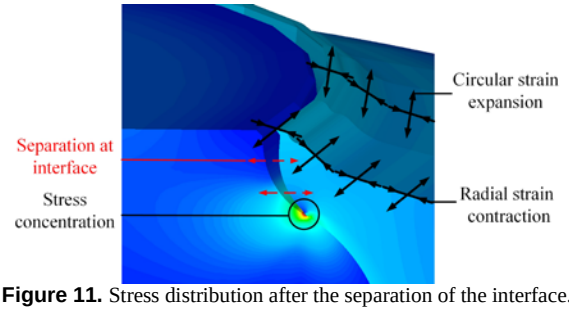

Figure 11. Stress distribution after the separation of the interface.

Once the interface failure occurs, the internal stress of the spacer and the hydraulic pressure will make the spacer move away from the center conductor under the concave surface loading because the constraint from the center conductor is lost, which will result in the separation of the center conductor and spacer. Figure 11 demonstrates the stress distribution near the interface with a separation.

As Figure 11 illustrates, the circular strain on the surface of spacer near the center conductor tends to expand and the radial strain tends to contract, thus a wedge air-gap is formed between the center conductor and the spacer. Once the wedge air-gap is formed, the stress is concentrated on the tip of the air-gap, which will continue to develop the extension of separation. With the increase of hydraulic pressure, the maximum stress at the tip will finally reach the failure strength of epoxy composite, leading to the cracks in spacer body near the interface, so that the epoxy composite cracks into small pieces at the surface of the spacer near the interface as Figure 5 shows. The cracks develop fast and finally damage the whole GIL insulator. Notably, the epoxy composite will loss the constraint from the aluminum when the separation occurs. In this case, the circular strain measured by C1 sensor near the center conductor will become larger and the radial strain measured by R1 sensor will become smaller after the interface separation, which verify the experimental results as the Figure 4 shows.

Through strain measurement and stress distribution calculation, it can be concluded that separation may occurs at the interface between the center conductor and spacer, which will introduce air-gaps at the interface.

5 EFFECT OF INTERFACE SEPARATION ON DIELECTRIC STRENGTH

The separation of the center conductor and epoxy composite of the GIL insulator in the hydrostatic test was introduced in last section, and the result shows that the internal stress by casting and applying single-side pressure on the surface of the spacer may lead to the separation of interface. During operation, the GIL insulator may face the same situation, airgaps will be generated at the interface between the center conductor and spacer, which will affect the electric field distribution of GIL insulator, even threating the safe operation of GIL. Therefore, the influence of interface separation on electric field distribution is studied by calculation. In addition, the simplified GIL insulator models are fabricated and the gas-solid interfacial flashover strengths of insulator model are studied by experiment.

5.1 EFFECT ON ELECTRIC FIELD DISTRIBUTION

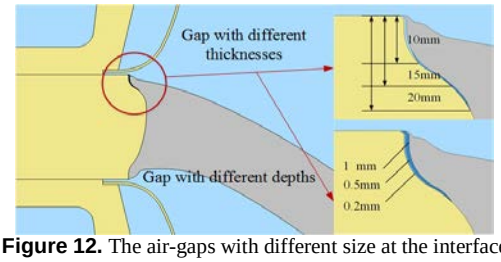

Figure 12. The air-gaps with different size at the interface

Gap models with different depths and thicknesses are established at the interface between the center conductor and spacer. Two kinds of gaps are established with a fixed thickness of 0.5 mm, depths of 10 mm, 15 mm and 20 mm respectively and with a fixed depth of 15 mm, thickness of 0.2 mm, 0.5 mm and 1 mm respectively as Figure 12 demonstrates.

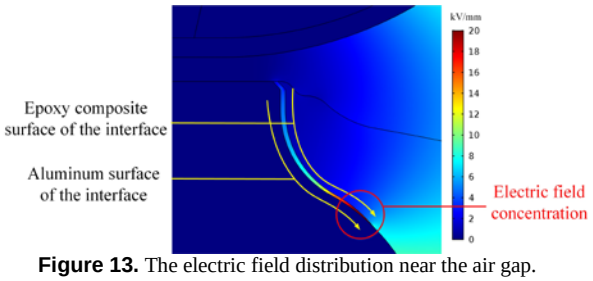

Figure 13. The electric field distribution near the air gap.

The calculation analyzes the electric field distribution of GIL insulators with interface air-gaps under lightning impulses voltage of 2400 kV, which is the most demanding situation in operation. The relative permittivity of epoxy composite and SF_6 is 5.5 and 1, respectively [24]. The electric field distribution near the air-gap with 15 mm in depth and 0.5 mm in thickness is shown in Figure 13.

Figure 13 shows that the existence of the air-gap distorts the electric field at the interface. There is a significant electric field concentration at the tip of the air-gap. The maximum electric field strength increases dramatically from convex surface of spacer toward inside, which may lead to the severe discharge at interface. In order to analyze the electric field distortion, air-gaps with different size is studied and the electric field strength on the aluminum surface and epoxy surface of the interface are obtained as in Figure 14.

Figure 14 shows that the electric field strength increases gradually from the convex surface to the center, and a rapid increase appears near the tip of air-gap, achieving the maximum value. The electric field on epoxy composite and metal surface of the interface shows a similar trend. Moreover, when the depth of gap is fixed, the maximum electric field strength of gaps with different thicknesses is almost similar. However, when the thickness of gaps is fixed, the deeper gap, the greater electric field strength at the tip of the gap.

The development of the interface separation will lead to the extension of air-gap, which will further distort the electric field. The concentration of electric field could initiate the partial discharge at the tips of the air-gaps. In addition, long-

term discharge may even cause electric erosion of the insulating materials, which will also further reduce the interfacial mechanical and dielectric strength. When the discharge work together with the concentrated mechanical stress, the extension speed of the air-gap will be further accelerated. More seriously, the discharge may develop along interface, leading to the severe flashover on the surface of the spacer.

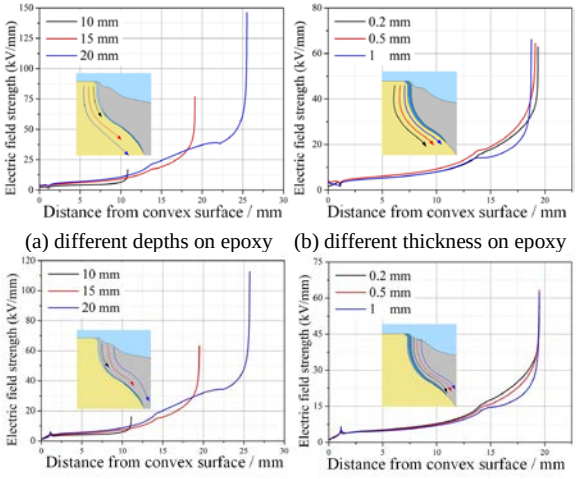

(a) different depths on epoxy (b) different thickness on epoxy

(c) different depths on metal (d) different thickness on metal

Figure 14. The air-gap with different size at the interface.

5.2 EFFECT ON FLASHOVER STRENGTH

In order to study the influence of interface separation on the flashover properties of GIL, GIL insulator is scaled down and simplified into disk type model, epoxy composite is coaxially cured on a cylindrical aluminum conductor. Accordingly, a steel sheet with thickness of 2 mm is arranged between the epoxy composite and aluminum, and an air-gap is generated by removing the sheet after curing. Two simplified insulator samples with and without air-gap are shown in Figure 15.

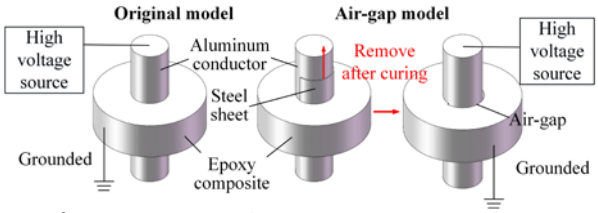

Figure 15. The simplified GIL insulator sample with air gap.

AC voltage is applied on the aluminum conductor and increased at 0.5 kV/s until flashover with the edge of the insulator model grounded. The original insulator model and the air-gap insulator model were subjected to 20 flashover tests.

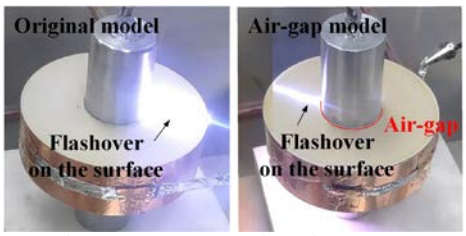

Figure 16. Flashover on the surface of the insulator model.

With the increase of voltage, PD eventually appears on the insulator model, and flashover finally takes place on the surface of the insulator model from the aluminum conductor towards the edge as Figure 16 shows. Before flashover occurs, the PD of air-gap model is more severe than the original model. The flashover voltage of each test is recorded, and a two-parameter Weibull statistic described as Equation (5) [25] is utilized to analyze the flashover strength of each sample.

$$F(V) = 1 - \exp\{-(V/\alpha)^{\beta}\} \tag{5}$$

where V is flashover voltage, $F(V)$ is the probability of failure at the flashover voltage less than or equal to V. The scale parameter α is associated with the flashover voltage for the failure probability of 63.2%. The shape parameter β is a measure of the range of flashover voltage, which reflects the dispersion degree of flashover voltage. As Figure 17 shows, the α of air-gap model is 27.85 kV, which is smaller than that of original model (30.98 kV), indicating that the introduction of the air-gap reduces the flashover strength of the insulator. Moreover, the β of air-gap model is smaller than the original one, suggesting largely reduced dielectric reliability is induced by the existence of air-gap.

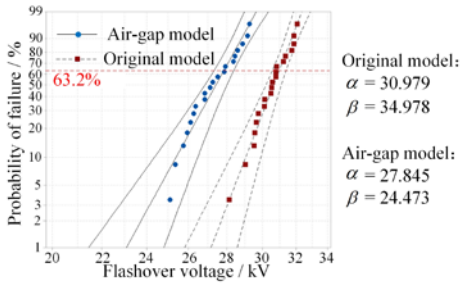

Figure 17. Weibull statistics of flashover voltage.

From the combination of the calculation and experimental results, it can be concluded that the existence of air-gap by interface separation will cause concentrated electric field at the interface between the center conductor and spacer as well as the reduced interfacial dielectric strengths of GIL insulator.

6 CONCLUSIONS

In this work, hydrostatic tests were conducted on GIL insulator to simulate the single-side pressure during operation and FBG sensors measured the strain on the surface of the spacer. FEM was used to analyze the stress distribution. In addition, the presence of an air gap on electric field distribution by calculation were studied based on the mechanical defects generated by interface separations. A simplified GIL insulator model with an air gap was used to study the gas-solid interfacial flashover strength.

During the hydraulic tests, an abnormality was found at 2.2 MPa load near the interface of the high voltage conductor and spacer. Combining with the failure morphology of GIL insulators, it can be inferred that the abnormality occurs near the interface. Calculations show the stress distribution of GIL insulators during casting and operation. The results indicate that there exists stress concentration at the interface between the center conductor and spacer. In addition, the results show that the shear stress also concentrates near the convex surface of spacer at the interface, which may lead to the interfacial separation between the center conductor and spacer from the

convex surface, and generate wedge air gaps at the interface. With increased stress, the air gap increase in size and distorts the electric field, which leads to electric field concentration at the tip of the air gap and PD. The model simulations indicate a reduced flashover voltage.

These experiments and calculations indicate stress concentration during casting and operation likely leads to interfacial separation of GIL insulators, a concentration of electric field and the reduction of surface flashover strength.

ACKNOWLEDGMENT

This work is supported by the Science and Technology Project of State Grid Corporation of China (SGTYHT/15-JS-191).

REFERENCES

[1] H. Koch, "Gas-insulated transmission line (GIL)," *IEEE Power Engineering Society General Meeting*, 2003, pp. 2480-2483.

[2] S. Poehler, P. Rudenko, "Directly buried gas-insulated transmission lines (GIL)," *IEEE/PES Transmission and Distribution Conf. Exposition (T&D)*, 2012, pp. 1-5.

[3] C. Li, J. He, J. Hu, "Surface morphology and electrical characteristics of direct fluorinated epoxy-resin/alumina composite," IEEE Trans. Dielectr. Electr. Insul., vol. 23, no. 5, pp. 3071-3077, 2016.

[4] H. Okubo, T. Hoshino, T. Takahashi, "Insulation design and on-site testing method for a long distance, gas insulated transmission line (GIL)," IEEE Electr. Insul. Mag., vol. 14, no 6, pp. 13-22, 1998.

[5] S. Okabe, "Insulation properties and degradation mechanism of insulating spacers in gas insulated switchgear (GIS) for repeated/long voltage application," IEEE Trans. Dielectr. Electr. Insul., vol. 14, no 1, pp. 101-110, 2007.

[6] H. Xiong, H. Jiang, B. Zhou, G. Zhou, "Research on an accident of 500 kV gas insulated transmission line," Appl. Mech. Mater., vol. 492, pp. 178-181, 2014.

[7] D. Mansour, H. Kojima, N. Hayakawa, F. Endo, H. Okubo, "Partial discharges and associated mechanisms for micro gap delamination at epoxy spacer in GIS," IEEE Trans. Dielectr. Electr. Insul., vol. 17, no. 3, pp. 855-861, 2010.

[8] D. Mansour, H. Kojima, N. Hayakawa, M. Hanai, H. Okubo, "Physical mechanisms of partial discharges at nitrogen filled delamination in epoxy cast resin power apparatus," IEEE Trans. Dielectr. Electr. Insul, vol. 20, no 2, pp. 454-461, 2013.

[9] G. Ueta, J. Wada, S. Okabe, M. Miyashita, C. Nishida, M. Kamei, "Insulation characteristics of epoxy insulator with internal crack-shaped micro-defects-fundamental study on breakdown mechanism," IEEE Trans. Dielectr. Electr. Insul., vol. 20, no. 4, pp. 1444-1451, 2013.

[10] G. Ueta, J. Wada, S. Okabe, M. Miyashita, C. Nishida, M. Kamei, "Insulation performance of three types of micro-defects in inner epoxy insulators," IEEE Trans. Dielectr. Electr. Insul., vol. 19, no. 3, pp. 947-954, 2012.

[11] T. Umemura, S. Nakamura, M. Hikita, T. Maeda, M. Higashiyama. "Partial discharges of small-air-gap in cast-resin insulation system", IEEE Trans. Dielectr. Electr. Insul, vol. 20, no 1, pp. 255-261, 2013.

[12] W. Yuan, The study of crack discharge in ultra-high voltage basin-type insulator, MS dissertation, North China Electric Power University 2014. (in Chinese)

[13] S. Epackachi, K. Dolatshahi, N. Oliveto, A. Reinhorn, "Mechanical behavior of electrical hollow composite post insulators: experimental and analytical study," Eng. Struct., vol. 93, pp. 129-141, 2015.

[14] Y. Chen, B. Cui, N. Wang, Y. Liu, Y. Wu, P. Chen, "Study of improving mechanical strength for 1100kV spacer insulator," High Voltage Apparatus. vol. 51, no. 7, pp. 52-56, 2015. (in Chinese)

[15] G. Pereira, M. McGugan, L. P. Mikkelsen, "Method for independent strain and temperature measurement in polymeric tensile test specimen using embedded FBG sensors," Polym. Test., vol. 50, pp. 125-134, 2016.

[16] W. Li, C. Cheng, Y. Lou, "Investigation of strain transmission of surface-bonded FBGs used as strain sensors." Sens. Actuators A, vol. 149, no. 2, pp. 201-207, 2009.

[17] R. Wu, B. Zheng, Z. Liu, P. He, Y. Tan, "Analysis on strain transfer of a pasted FBG strain sensor," Optik, vol. 125, no. 18, pp. 4924-4928, 2014.

[18] H. Wang, Z. Guo, H. Feng, L. Liu, H. Tian, C. Wang, Z. Peng, "Simulation and experimental study on mechanical performance of UHV GIS spacer in hydrostatic test," IEEE Trans. Dielectr. Electr. Insul., vol. 24, no. 5, pp. 3122-3131, 2017.

[19] H. Wang, Z. Guo, Q. Wang, C. Wang, H. Li, Z. Peng, "Experimental study on curing strain of epoxy-alumina composite applied to UHV GIS spacer," *IEEE Conf. Prop. Appl. Dielectr. Mater. (ICPADM)*, 2015, pp. 680-683.

[20] B. Li, *SF_6 high voltage electrical design*. Mechanical Industry Press 2015.

[21] P. R. Marur, R. C. Batra, G. Garcia, A. C. Loos, "Static and dynamic fracture toughness of epoxy/alumina composite with submicron inclusions," J. Mater. Sci., vol. 39, no. 4, pp. 1437-1440, 2004.

[22] C. Wang, H. Li, H. Zhang, H. Wang, L. Liu, Z. Xu, P. Liu, Z. Peng, "Influence of addition of hydroxyl-terminated liquid nitrile rubber on dielectric properties and relaxation behavior of epoxy resin," IEEE Trans. Dielectr. Electr. Insul., vol. 23, no. 4, pp. 2258-2269, 2016.

[23] H. Li, C. Wang, Z. Guo, H. Wang, S. Zhang, Z. Peng, F. Ma, "Influences of semiconductive coatings on the electric field distribution of GIS spacer interface," *IEEE Conf. Prop. Appl. Dielectr. Mater. (ICPADM)*, 2015, pp. 887-890.

[24] H. Ji, C. Li, G. Ma, Z. Pang, Z. Tang, H. Wen, B. Cui, "Partial discharge occurrence induced by crack defect on GIS insulator operated at 1100 kV," IEEE Trans. Dielectr. Electr. Insul., vol. 23, no. 4, pp. 2250-2257, 2016.

[25] H. Li, F. Liu, H. Tian, C. Wang, Z. Guo, P. Liu, Z. Peng, Q. Wang, "Synergetic enhancement of mechanical and electrical strength in epoxy/silica nanocomposites via chemically-bonded interface," Compos. Sci. Technol., vol. 167, pp. 539-546, 2018.

Zihao Guo was born in Shannxi, China, in 1991. He received the B.Eng. degree in Electrical Engineering from Xi'an Jiaotong University in 2013. Currently, he is working for Ph. D. degree in the School of Electrical Engineering at Xi'an Jiaotong University. His main research interests include high-voltage and insulation technology, electrical and mechanical properties of UVH power equipment such as GIS/GIL spacer.

Zongren Peng was born in Shaanxi, China. He graduated from Xi'an Jiaotong University, China, in 1977, majoring in Electrical Engineering. He is a Professor of Electrical Engineering at Xi'an Jiaotong University. His research fields include the calculation and the optimization of insulation structures for UHV power equipment, polymeric insulating materials, measurement of space charges in high-voltage insulation systems. He is a Distinguished Expert in SGCC (State Grid Corporation of China). He can be reached by email at zrpeng@xjtu.edu.cn.

Qing Wang was born in Hubei, China. He received the Ph.D. degree in Chemistry from The University of Chicago, in 2000. He is a Professor of Materials Science and Engineering at the Pennsylvania State University, University Park, PA, USA. His research interests are centered on the development of functional materials including ferroelectric polymers, electroactive polymers and polymer–ceramic nanocomposites for applications in electronics, power equipment, energy storage and energy harvesting. He can be reached by email at wang@matse.psu.edu.